Contents

Chapter 4

Photon Beam

One of the unique opportunities presented by a CEBAF upgrade to energies of 8 GeV and beyond is the possibility of generating high-intensity c.w. photon beams for high energy photoproduction experiments. In this regime, photon beams represent an interesting extension to the meson spectroscopy program that has been actively pursued using beams of pseudoscalar mesons at hadron accelerator laboratories: with high energy photons one has essentially a bam of *vector* mesons. It is difficult, in fact, to conceive of any other way to obtain such a vector beam.

Vector beams offer at least two advantages in the search for a more complete understanding of the hadron spectrum. From the theoretical standpoint, vectors are interesting as a possible source of hybrid mesons because the two are connected in the flux tube model by a simple operator which excited the orbital motion of the flux tube. Thus, measuring the coupling between conventional and hybrid mesons is a direct way to probe the structure of hybrids. From the experimental point of view, the polarization of a vector beam offers new observables that are not available to experiments with pseudoscalar beams. These additional observables are useful to distinguish the exchange character of the production process and help resolve contributions from different interfering waves in the partial wave analysis of the final state.

4.1 Choice of technique

Three major methods have been considered for producing photons of the highest possible energy, flux and polarization from electrons in the energy range 8-12 GeV. The methods are ordinary bremsstrahlung, coherent bremsstrahlung and Compton backscattering of light. None of the methods are new and cal-

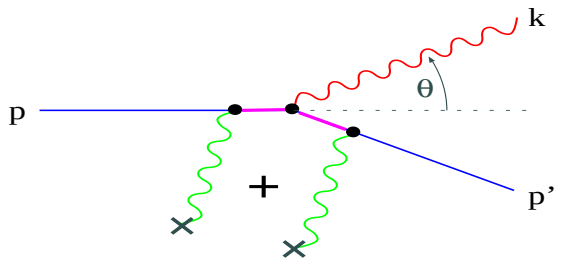

Figure 4.1: Generic diagrams for hard photon production from a high energy electron beam. The symbol $\times$ represents either a static charge distribution, in the case of virtual photons in the initial state (i.e. bremsstrahlung) or an optical cavity, in the case of real photons in the initial state (i.e. Compton scattering) The + denotes the fact that this leading order amplitude is actually the sum of two diagrams, one with the initial state photons attached to the incoming electron leg and one with it attached to the outgoing electron.

culation of the basic cross sections that underlie them are presented in most textbooks on applications of QED. All three techniques are actually described by the same Feynman diagram shown in figure 4.1

Each of these techniques has its own limitations and advantages. This, taken together with the requirements of the experimental program determine the method used to generate the photon beam. The experimental requirements (beam energy and polarization) are discussed below followed by a brief discussion of the properties of Compton backscattered and ordinary bremsstrahlung beams. The coherent bremsstrahlung technique is clearly the best choice to satisfy the requirements of the experimental program and this solution is then discussed in detail.

4.2 Energy requirements

The interesting range of meson masses for the study of gluonic excitations spans the region from the mass of the π^0 to just below $c\bar{c}$ threshold ($\approx$ 3 GeV/c^2). This range includes conventional ($q\bar{q}$) mesons and glueball and exotic hybrid masses, as predicted by lattice gauge calculations, flux tube models and bag models.

Figure 4.2 shows the maximum mass of particle X, in the reaction $\gamma p \rightarrow Xp$

as a function of incident photon energy. As can be seen from this plot, the desired mass range could be achieved with photon energies below ≈ 8 GeV. However higher energies are needed to produce mesons with sufficient boost so as to achieve good acceptance for the decay products of produced resonances.

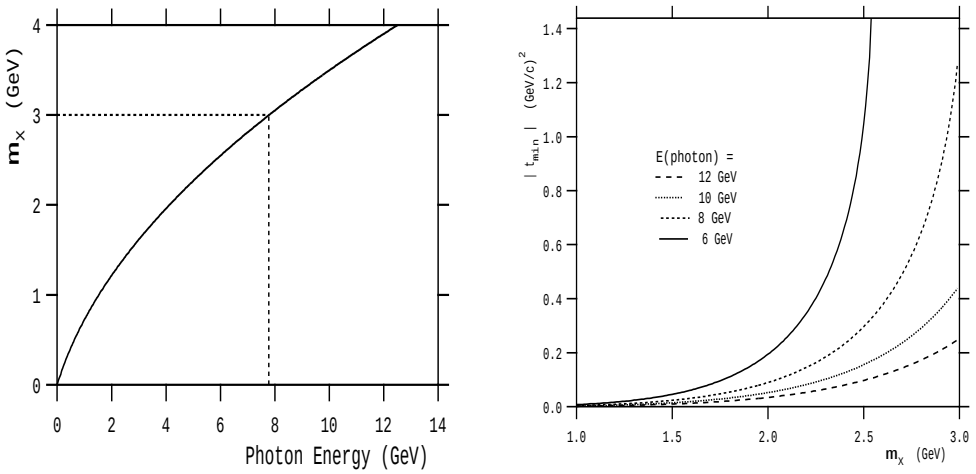

Figure 4.2: Kinematic limits on production properties for several choices of beam energy. (left) Maximum mass for particle X as a function of incident photon energy in the reaction $\gamma p \to Xp$. (right) The minimum value of $|t|$ as a function of the mass of particle X in the reaction $\gamma p \to Xp$ for various values of incident photon energies.

Higher energies are also needed to minimize the effect of the overlap of produced baryon resonances with meson resonances. This is illustrated by the Dalitz plot boundaries of Figure 4.3 for the reactions $\gamma p \to \pi\pi p$ and $\gamma p \to \eta\eta p$ for various incident photon energies. As the incident energy is increased from 4 to 8 to 12 GeV, the effect of overlap of produced mesons with produced baryon resonances (N^* or Δ) becomes less important.

Another important consideration in choice of energy is the effect of the minimum square of the momentum transfer, $|t_{min}|$ from incoming photon to outgoing meson required in the reaction $\gamma p \to Xp$. The dependence of $|t_{min}|$ on the mass of X is shown in Figure 4.2 for various incident photon energies.

The effect of $|t_{min}|$ can be illustrated in the production rate of mesons in peripheral processes. Figure 4.4 shows the mass spectrum of the meson system X in the reaction $\gamma p \to Xp$. Resonances with equal cross-sections are assumed but weighted by $dN/dt = e^{-8\cdot|t|}$. Resonance widths were all chosen to be 100 MeV/c^2 with masses of 1.0, 1.5, 2.0 and 2.5 GeV/c^2 for incident photon energies of 6, 8, 10, and 12 GeV. Clearly, photon beam energies of $\approx$

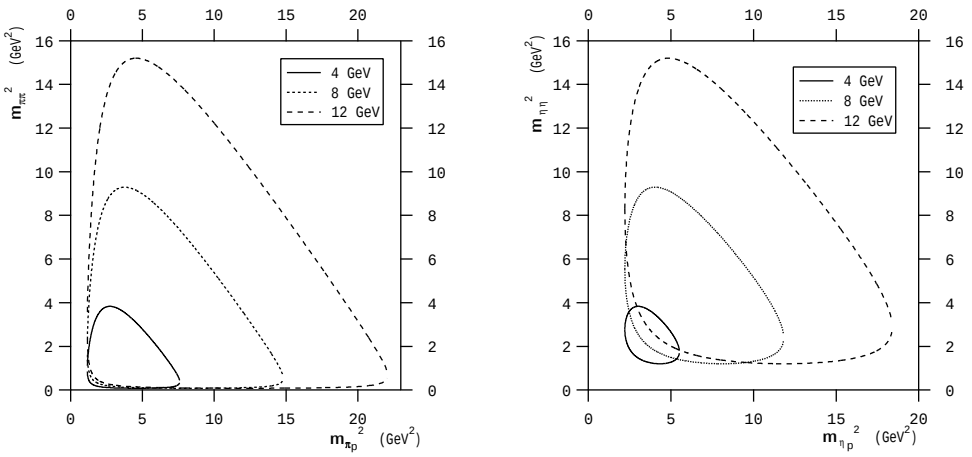

Figure 4.3: Dalitz plot boundaries for the reaction $\gamma p \to \pi\pi p$ (left) and $\gamma p \to \eta\eta p$ (right) for incident photon energies of 4, 8 and 12 GeV.

12 GeV are required if the mass region up to 3 GeV/c^2 is to be studied.

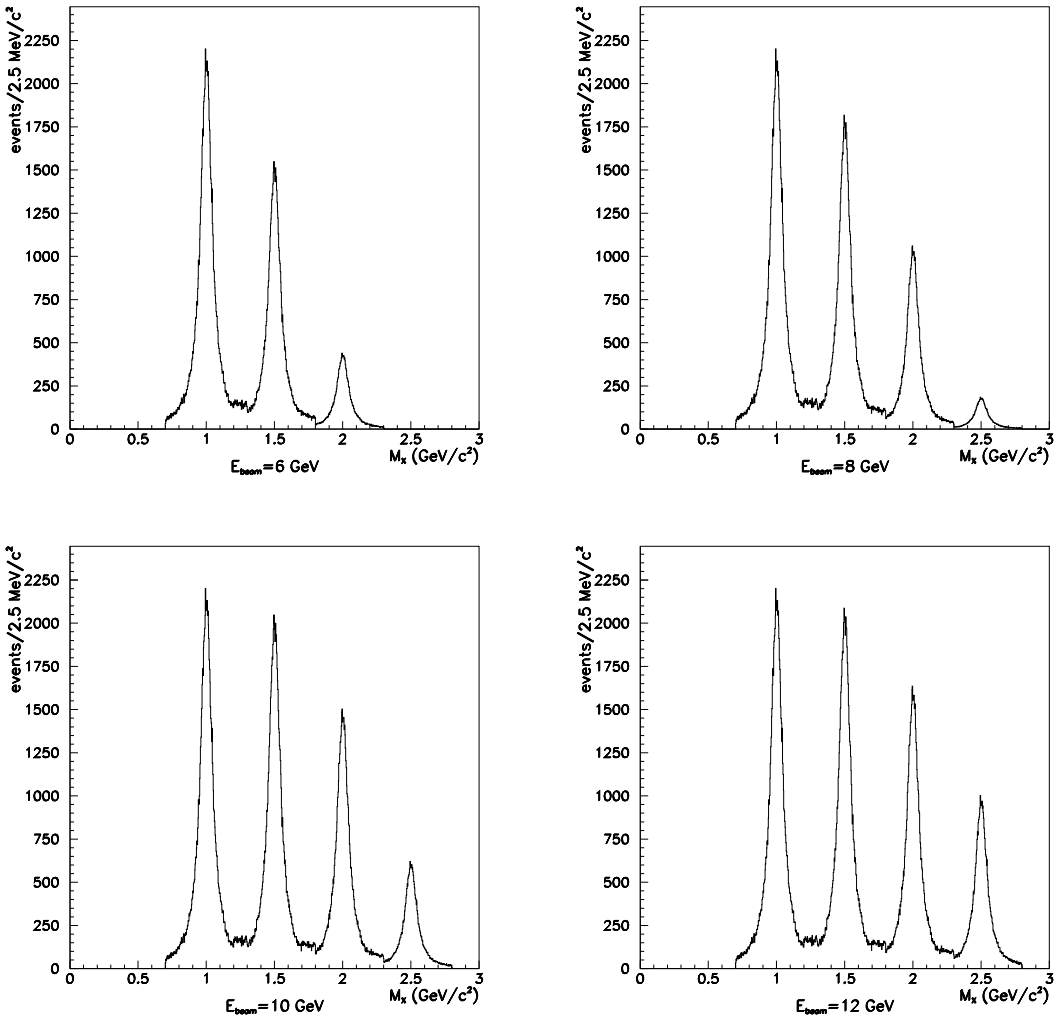

Figure 4.4: Plots of the mass distribution of 4 produced resonances in the reaction $\gamma p \to Xp$ taking into account the t_{min} effect for an incident photon energy of 6 GeV (upper left), 8 GeV (upper right), 10 GeV (lower left) and 12 GeV (lower right). (see the text for details).

4.3 Polarization requirements

From the point of view of physics of the HALL D the main difference between photon and hadron beams has to do with their quark content. With a good accuracy, photons may be viewed as a superposition of spin-1 $q\bar{q}$-pairs while a typical hadronic beam of pions or kaons is a source of valence spin-0 $q\bar{q}$ pairs. Thus, as compared to hadroproduction, photons may lead to different final states or similar final states may be reached via different production mechanisms. This unique quark structure of the photon might be of particular relevance for production of exotic states. This is because for low lying exotics theory predicts their valence $q\bar{q}$ pair to be in the spin-1 configuration [1].

The basic mechanisms of meson photoproduction are through diffraction, t-channel meson exchange and a decay of an excited baryonic resonance. From these three, at HALL D energies t-channel exchanges dominate. The hierarchy of exchanges suppresses those which require a change of several quantum numbers at once. Thus from the possible t-channel exchange the Pomeron exchange followed by a charge exchange are expected to dominate. Nevertheless at energies available at HALL D an extensive coverage of various production mechanisms is expected [2]. Real photons have two, transverse degrees of polarization and therefore are "richer" then π or K beams. This is reflected in the number of independent spin-density matrix elements. For example in photoproduction of vector mesons on an unpolarized proton target, $\gamma p \to VN$ there are 17 independent real spin-density matrix elements. For comparison, an analogous reaction with pion beams, $\pi p \to VN$ has only 4 independent real parameters in the spin-density matrix. Dynamical content of photoproduction is clearly larger. The crucial point however is how many of the spin-density matrix elements can actually be measured. In general this number depends on the type of photon polarization. In the above example if the vector meson is analyzed via its two body, (pseudo)scalar decay, *e.g.* $V = \rho \to 2\pi$ or $V = \phi \to K\bar{K}$ then linearly, circularly, and unpolarized photons access 9, 5, and 3 out of the 17 spin matrix elements, respectively [3]. In general linear polarization enables to extract the largest number of the spin-density matrix elements.

When t-channel exchanges dominate, linear polarization is even more important since it enables to isolate natural from unnatural parity exchanges. Naturality, τ of a state with intrinsic parity, η and spin J is defined as a product $\tau = \eta(-)^J$. Thus, for example the $\pi(J^{PC} = 0^{-+})$ and $a_1(J^{PC} = 1^{++})$ are unnatural, while the $\rho(J^{PC} = 1^{--})$ or the exotic $\hat{\rho}(J^{PC} = 1^{-+})$ are natural. Measurement of naturality of the exchanged particle together with its t-dependence and partial wave analysis are central for identification of pro-

duced mesonic resonances and understanding of production mechanisms. To see the connection between photon polarization and naturality in the t-channel consider a reaction $a+b \to c+d$ where a, b refer to the beam and target particle respectively and c, d to the produced meson and the recoiling baryon. We will assume that t-channel exchange of a particle, e or more generally of a Reggion dominates. This type of processes are best analyzed in the Gottfried-Jackson frame defined as the rest frame of the produced meson, (particle c) with the spin quantization, z-axis chosen in the direction of the beam (particle a) in that frame. Consider the case of pion beam first. It is possible to show that symmetry of the corresponding production amplitude $A(m_c) = A_{a+b\to c+d}$ under interchange $m_c \to -m_c$, where m_c is the spin projection of the produced meson (target and the recoiling baryon spins are implicit since they are irrelevant in the following discussion) is determined by the product of naturalities of the exchanged particle (τ_e) and that of the produced meson (τ_c). Thus, for a final state of given naturality, (say $\tau_c = +1$) determined by a partial wave $A(m_c)$ the two combinations

$$A^{U,N}(m_c) = \frac{1}{2}(A(m_c) \pm A(-m_c)) \tag{4.1}$$

isolate processes of opposite naturalities in the t-channel (if $\tau_c = -1$, A^U and A^N should be exchanged). For a photon beam an analogous partial wave, $A(m_a, m_c) = A_{a+b\to c+d}$ depends on the photon polarization, $m_a = \pm 1$. In this case when defining amplitudes which project onto definite naturality of the exchanged particle will also require flipping photon polarization (which is identical to photon helicity in the GJ frame). For $\tau_c = +1$ the corresponding two amplitudes are

$$A^{N,U}(m_c) = \frac{1}{2}(A(1, m_c) \pm A(-1, -m_c)) \tag{4.2}$$

with the definitions being reversed for $\tau_c = -1$. It thus follows that amplitudes with defined photon helicity *i.e.* corresponding to circularly polarized beams mix exchanges of different naturalities,

$$A(\pm 1, \pm m_c) = (A^N(m_c) \pm A^U(m_c)), \tag{4.3}$$

and to separate naturality of the exchanged particle it is necessary to measure coherent superpositions of the two helicity amplitudes. This can be achieved using linear polarization [3].

Finally lets focus on photoproduction of a $\hat{\rho}(J^{PC} = 1^{-+})$ exotic in a charge exchange reaction, $\gamma p \to \hat{\rho} n$ [4]. As discussed earlier, at HALL D energies one would expect diffractive photoproduction to dominate the total γp cross

section. However, since diffraction corresponds to a $C = +$ exchange the 1^{-+} exotic will not be product this way. Charge exchange is the next, least suppressed production mechanism, and since $\gamma\hat{\rho}\pi$ coupling is not ruled out by any symmetry, at low t pion exchange is expected to dominate. This is good news since OPE is reasonably well understood at high energies. In this case linear polarization has another advantage. One can show that in the GJ frame the photoproduction amplitude $A(m_a, m_c)$ is proportional to either $\delta_{m_a m_c}$ or $\tau^3_{m_a m_c}$ depending on the naturality of the produced meson [5]. Thus in this case linear polarization selects naturality of the produced mesonic resonance. For a *natural* exotic, 1^{-+} state with mass around 1.5-1.6 GeV/c^2, as seen in the E852 data [6], the dominant backgrounds are expected from the *unnatural* $a_1(1260)$ and $\pi_2(1670)$ ($a_2(1320)$ is too narrow to significantly contribute in this mass region). Thus direction of linear polarization of the exotic signal is then expected to be at 90^o with respect to the backgrounds. This has obvious implications for the partial wave analysis.

4.4 Compton backscattered beams

The basic design of the Compton-backscatter source for this study was taken from C. Keppel and R. Ent [7]. The design entails the use of a four mirror high-gain cavity pumped by a 10 kW argon0ion laser putting out 2 *ps* pulses at a frequency of 100 MHz. The pulses in the cavity are synchronized so that light pulses in each of the arms crossing the electron beam intercepts an electron bucket on each pass through the beam. The total length of the cavity is 2m with a crossing angle of 1°. Both cavity and electron beam are focused to $10\mu m$ r.m.s. radius at the crossing point and ideal alignment is assumed making this a technically challenging device to implement. Even so, and using the best dielectric mirrors now available, this source suffers from flux limitations. Figure 4.5 shows the photon energy spectrum in photons/GeV/s for a 1μA electron beam. The highest energy photons in this beam are only 30% of the endpoint energy.

Higher energies can be obtained by frequency doubling the laser before injection into the cavity. The spectrum and flux under these conditions is shown in figure 4.6. The observed losses in intensity arise from poorer mirror reflectivity at shorter wavelengths, inefficiency of the frequency doubling apparatus and the dropping Compton cross section with increasing photon energy. The endpoint energy is still less than 50% of the electron energy and well below the energy requirements described above, hence, this option is not considered further.

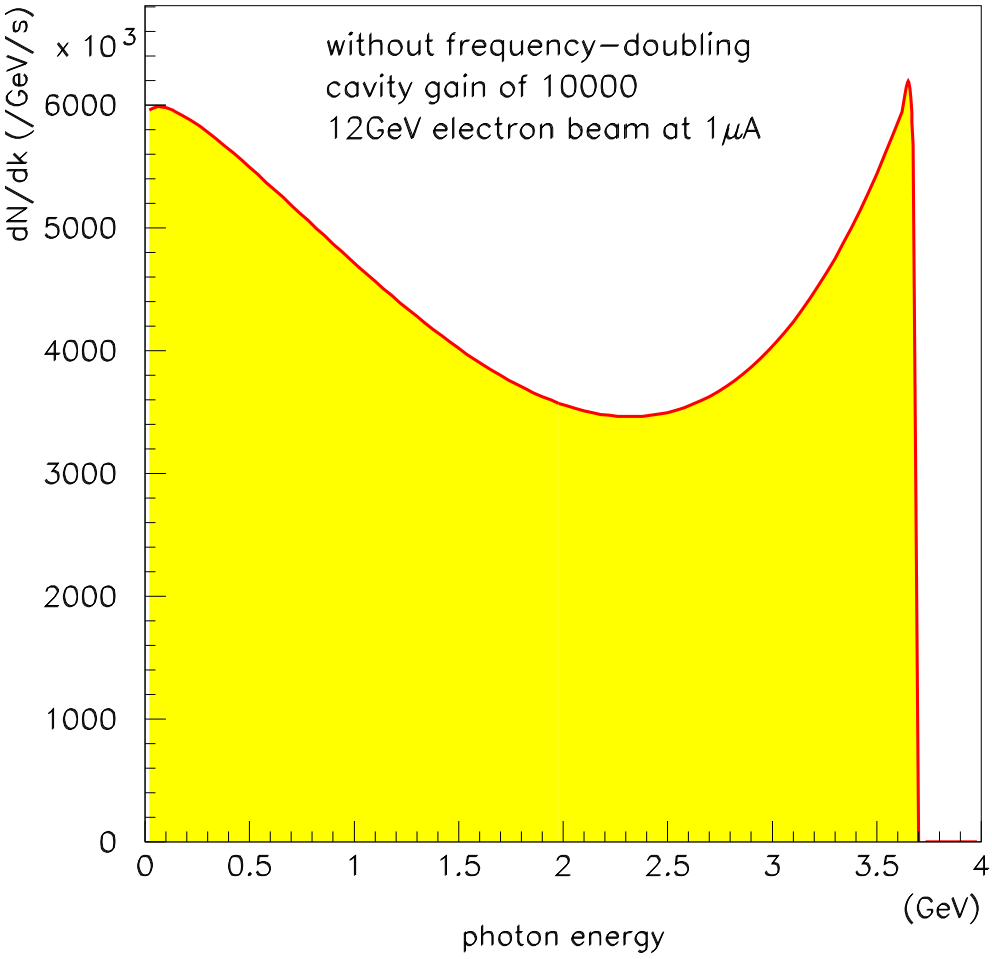

Figure 4.5: Photon energy spectrum in a laser backscatter photon beam for a resonant cavity driven by a state-of-the-art pulsed Argon-ion laser operating at 514 nm that is synchronized with the pulse cycle of the accelerator.

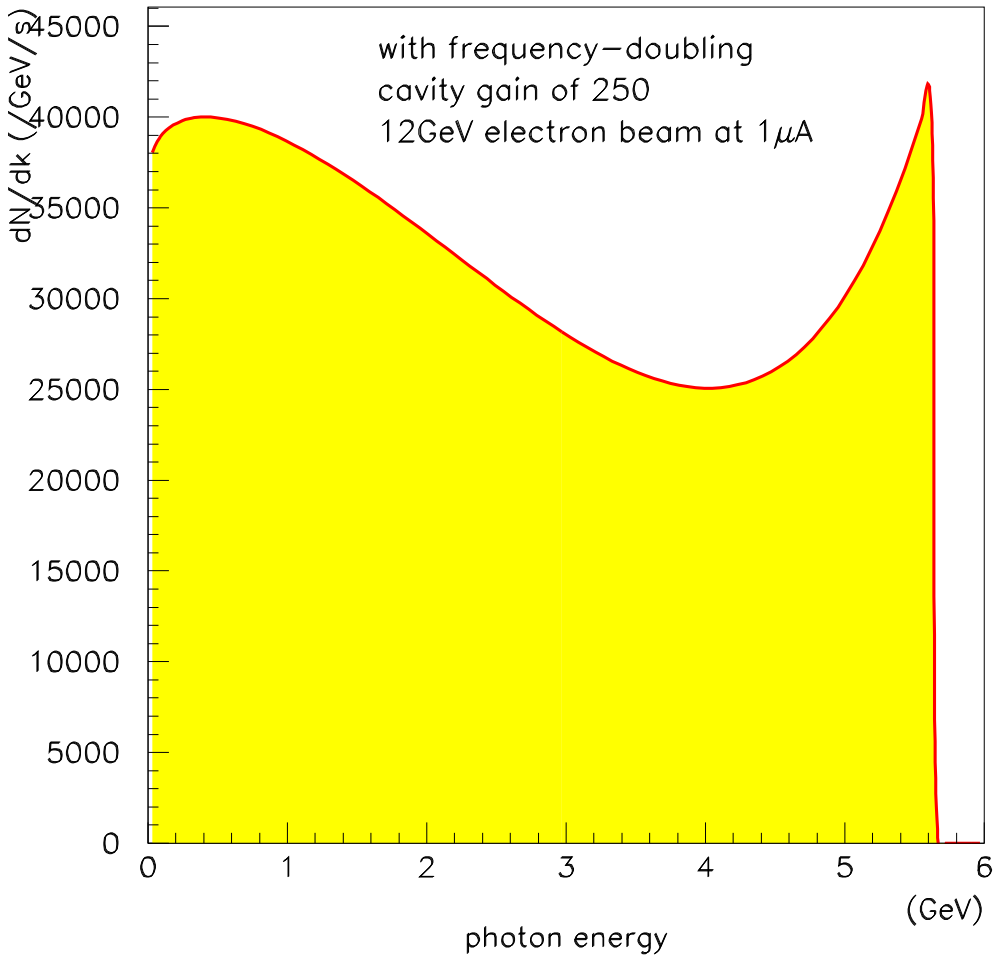

Figure 4.6: Same as figure 4.5 but using a frequency-doubler cavity tuned to 257 nm.

4.5 Bremsstrahlung beams

Bremsstrahlung offers the only practical way, starting with an electron beam at CEBAF energies, to produce a photon beam with a significant flux in the vicinity of the end point. Bremsstrahlung provides a naturally collimated photon beam with a characteristic angular spread of m/E, which allows the low emittance of the CEBAF beam to be effectively transfered into the secondary photon beam. Detecting the post-bremsstrahlung electron in a spectrometer in coincidence with the final state from photon interactions tags the energy of the incident photon, thereby providing an effectively monochromatic photon beam. The photons can be generated with a significant plane polarization by using a thin oriented crystal in the place of an amorphous or polycrystalline bremsstrahlung target (radiator), through the process of coherent bremsstrahlung. This polarization is enhanced by collimating the photon beam beyond its intrinsic angular spread, and making up the diminished flux by increasing the electron beam current. As shown below, even in the case of very thin crystals and severe collimation, the electron beam current required to satisfy the needs of this experiment is quite modest compared to what CEBAF can produce, which is why the facility can be located above ground. The experiment does, however, make significant demands on the machine from the point of view of emittance and beam position stability, both areas in which CEBAF has shown outstanding performance. In the following sections it is shown how the electron beam quality at higher energies translates into the quality of the photon beam available to the experiment.

A horizontal plan view of the photon beam line is shown in figure 4.7 with the major components labeled. The electron beam enters the figure from below ground at the left and is bent into the horizontal plane to enter the tagger building. There it passes through two small dipoles to impinge upon the bremsstrahlung radiator. After its exit from the radiator, the electron beam passes into the tagger magnet where the primary beam is bent in the direction of the electron beam dump. The radiator crystal is thin enough that most of the electrons lose less energy in traversing the radiator than the intrinsic energy spread of the incident beam, so apart from some emittance growth from multiple scattering in the radiator the primary beam is simply deflected by the tagger magnet into the dump. Those electrons which lose a significant fraction of their initial energy inside the radiator do so dominantly by emitting a single bremsstrahlung photon. These degraded electrons are bent out of the primary beam inside the tagger magnet and exit the vacuum between the poles of the magnet, passing through air for a short distance to strike the focal plane of the spectrometer. The primary electron beam is

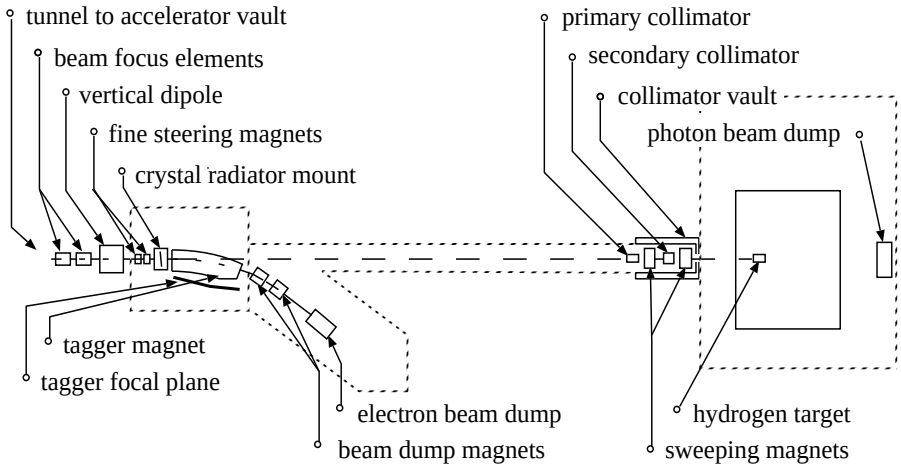

Figure 4.7: Schematic plan view of the photon beam line, shown in the horizontal plane as viewed from above. The objects in this figure are not drawn to scale.

contained inside vacuum all the way to the dump. The two dipole magnets shown in the figure downstream of the tagger are there to provide sufficient deflection that the dumping beam is not able to produce any forward-going particles into the experimental hall.

The photons that are produced in the radiator pass through the tagger magnet to exit the vacuum through a thin window in the forward direction. They then pass into a transfer pipe, which may either be evacuated or filled with helium to reduce photon beam degradation due to interactions, and travel to the experimental hall. Just before it enters the hall, the photon beam passes through a system of collimators and sweeping magnets housed inside a shielded vault. The primary collimator is first, defining the part of the photon beam that is allowed to reach the target. Debris from interactions that take place along the inside surface of the collimator forms a halo around the collimated photon beam. The charged component of the halo is deflected away from the beam axis by a dipole "sweeping" magnet just downstream of the collimator. A secondary collimator follows the sweeping magnet to stop the deflected shower particles and block the secondary photons generated from the first collimator. The secondary collimator is of larger diameter than the primary and so sees a reduced rate of secondary interactions on the inner surface of the hole, and what new showers are generated there are cleaned up by a second sweeping magnet and a final collimating aperture, through which the beam passes into

the experimental hall. This triple-collimation system was copied from the setup developed at SLAC [8].

The collimated photon beam, now only a few mm in diameter, is delivered to the experimental target. After passing through of order 5% radiation lengths of target, including windows and liquid hydrogen, the photon beam passes through the detector and into the photon beam dump at the back of the hall. The total power in the photon beam is at most 1W in the experimental hall, compared to at most 50W in the collimator vault, and 120kW maximum at the electron beam dump.

4.6 Photon Source

Essential features

The adjective 'coherent' in coherent bremsstrahlung does not indicate that the photons in the beam are in a coherent state, as is light from a laser. Rather it refers to the coherent effect of multiple atoms in a crystal lattice in absorbing the recoil momentum from a high energy electron when it radiates a bremsstrahlung photon. In X-ray spectroscopy one encounters the same thing in the Mosbauer effect, except in that case the chief physical consequence is the disappearance of the recoil Doppler shift. Here the chief consequence is the enhancement of bremsstrahlung at those particular kinematics for which the recoil momentum matches one of the reciprocal lattice vectors of the crystal. Another useful way to view the process of coherent bremsstrahlung is as virtual Compton scattering. To the high energy electron, the atoms in the radiator appear as clouds of virtual photons. For a disoriented radiator material, the virtual photon spectrum is given simply by the atomic form factor, averaged over the different species in the material. If the radiator is a single crystal, however, the atomic form factor gets multiplied by the form factor of the crystal, which in the ideal case looks like a series of delta-functions located at the sites of the reciprocal lattice. In effect, the crystal provides a set of virtual laser beams, each one a standing wave tuned to a specific reciprocal lattice vector. In this view the process of hard bremsstrahlung is seen to be the same as Compton backscattering of laser light. For a more detailed discussion of the physics of coherent bremsstrahlung there are a number of good references

The use of Compton backscattering of laser light as a photon source was earlier noted as ruled out by the limitation of high-power lasers and cavities to wavelengths above $100\mu m$. The characteristic wavelength of the crystal photons is a few Angstroms, three orders of magnitude shorter. In this case,

180° scattering would result in essentially 100% of the electron beam momentum being transfered to the photon in the lab frame. Unfortunately, however, the Compton cross section contains a factor of $(\vec{q} \cdot \vec{p})^2$ where $\vec{q}$ is the virtual photon momentum and $\vec{p}$ is that of the electron, which strongly favors incident photons with $\vec{q}$ nearly orthogonal to $\vec{p}$. With reciprocal lattice vectors pointing in almost every direction, only those nearly perpendicular to the beam contribute appreciably to the scattering rate. This fact applies equally to ordinary bremsstrahlung; in fact, to a first approximation the bremsstrahlung spectrum from a single crystal is the same as from a disoriented radiator. The reason is that, if the sum over crystal momenta were replaced with a continuous integral, one would recover the ordinary bremsstrahlung result for isolated atoms. Beyond a few unit cells from the origin in reciprocal lattice space, the atomic form factor and kinematic factors become slowly varying on the scale of the lattice spacing, and the sum becomes indistinguishable from the integral. Besides that, the uncertainty principle requires that atoms localized at the sites in a crystal undergo fluctuations about their mean position. This has the effect of attenuating the discrete peaks in the crystal form factor at progressively higher-order crystal momenta, eventually washing them out and filling in the gaps between them, so that the sum deforms smoothly into the integral at high momentum transfer. Hence, the sum over crystal indices that yields the final photon spectrum can be separated into two parts: a discrete sum over a limited set of small crystal indices and an integral over the continuum of momentum transfer values beyond. The latter appears in the coherent bremsstrahlung beam as an ordinary $1/k$ bremsstrahlung spectrum, while the former appears as a set of peak structures superimposed upon it. The $1/k$ continuum, referred to as the incoherent component, is invariant as the crystal is rotated, whereas the coherent peaks change in position and intensity, depending on crystal orientation.

A typical coherent bremsstrahlung spectrum is shown in figure 4.8. The distinction between incoherent and coherent components in the figure is artificial; it is there to show the part of the spectrum that shifts as the crystal is rotated. The vertical scale in the figure gives the photon rate for the given beam current and crystal thickness. Note that the intensity of the incoherent background is less than what would be obtained with an amorphous carbon radiator of the same thickness, because a part of the momentum transfer integral in the Bethe-Heitler formula has been moved into the discrete sum and contributes to the coherent part. The radiation length of diamond is actually an average over all orientations of the crystal. In the calculation for figure 4.8 the leading 400 lattice sites were included in the discrete part of the calculation, although it can be seen that only two or three of them contribute with

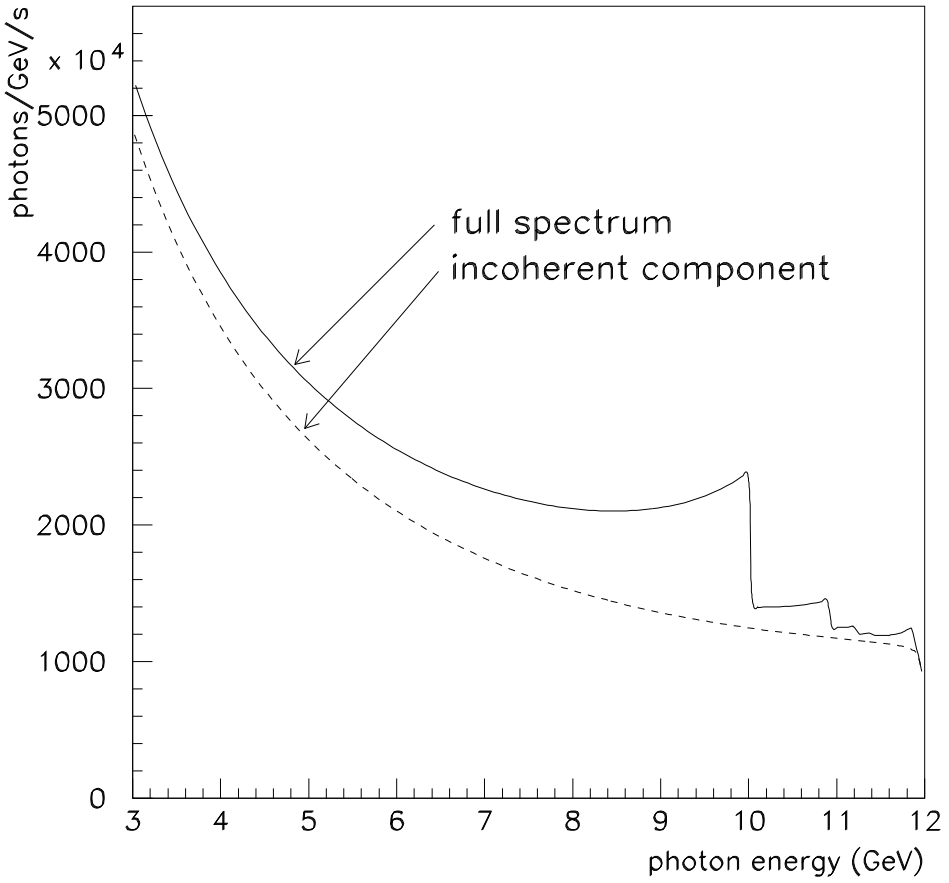

Figure 4.8: Coherent bremsstrahlung spectrum, calculated for a diamond crystal radiator $20\mu m$ thick and a 100nA electron beam of 12 GeV energy. Typical values were used for beam emittance and crystal mosaic spread.

sufficient intensity to be individually visible in the spectrum.

4.6.1 Use of collimation

The presence of the large incoherent flux in 4.8 presents a significant handicap to a photoproduction experiment. Not only do the low energy photons produce background in the detector, but they diminish the polarization of the beam. The entire beam polarization appears in the coherent component; the underlying incoherent flux only serves to dilute the polarization. There is another difference between the two components that allows them to be separated to some extent. The kinematics of bremsstrahlung confines most of the intensity of the photon beam to forward angles within m/E radians of the incident electron direction. In the lab this is a small angle, but in the rest frame of the electron-photon system it subtends all angles in the forward hemisphere. A peak in the coherent component that corresponds to a single reciprocal lattice vector has two-body kinematics, so there is a well-defined relation between the emission angle and the energy of the emitted photon in the lab: emission at 0° yields a maximum energy photon, with energy decreasing with increasing angle. This accounts for the shape of the coherent peaks in figure 4.8, with the sharp right-hand edge corresponding to 0° emission and the tail to lower energies corresponding to scattering into higher angles.

The incoherent component, because it comes from a sum over momentum transfers at all angles, has essentially no correlation between photon energy and emission angle. This means that collimating away all photons beyond some angle $\theta_{max} < m/E$ uniformly attenuates the incoherent spectrum at all energies, whereas it preserves all of the coherent photons from the maximum energy for the given peak down to some cutoff. The kinematic relations for coherent bremsstrahlung are as follows,

$$\theta^2 + 1 = \left(\frac{1-x}{x}\right)\left(\frac{x_{max}}{1-x_{max}}\right) \tag{4.4}$$

$$x_{max} = \frac{2\vec{p}\cdot\vec{q}}{2\vec{p}\cdot\vec{q} - m_e^2} \tag{4.5}$$

where x is the photon energy in units of the incident electron energy and θ is the lab emission angle of the photon relative to the incident electron momentum axis, in units of m/E .

The effects of collimation are demonstrated in the calculated spectra shown in figure 4.9. First, note that the collimation angles are very small, which requires a long flight path of order 100m in order that the collimator can be

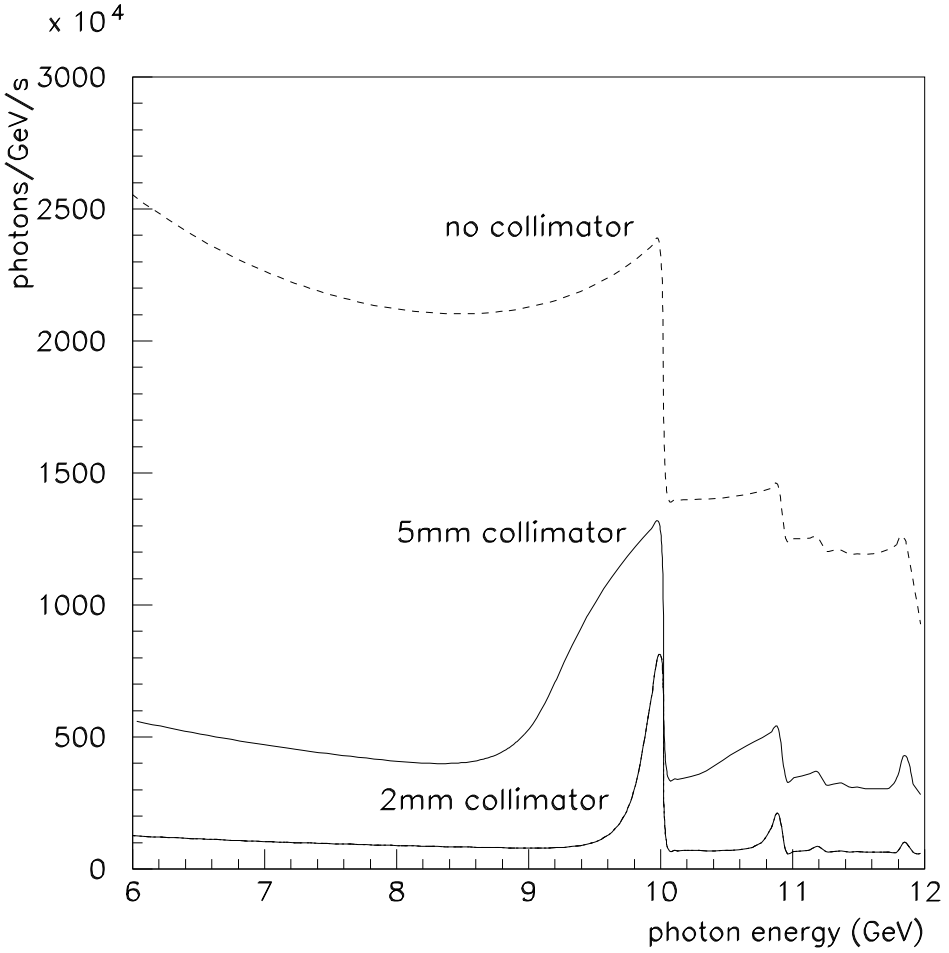

Figure 4.9: Coherent bremsstrahlung spectrum, calculated under the same conditions as in figure 4.8 , after collimation. The upper curve is the uncollimated spectrum from figure 4.8. The middle curve corresponds to a $5mm$ diameter collimator placed 80m downstream of the radiator, or approximately 0.75 m/E in collimator half-angle. The lower curve corresponds to a $2mm$ collimator in the same position, approximately 0.30 m/E in half-angle.

larger than the intrinsic beam spot size, otherwise the collimator is cutting in transverse coordinate instead of in angle. This distance is, in fact, a sensitive function of the electron beam emittance from the machine, and must be increased in inverse proportion to the beam emittance if the effectiveness of collimation is to be maintained. This issue, along with the associated demands placed on beam alignment and position stability, are taken up in more detail in the following section on the electron beam line.

Second, note that the cut imposed on the coherent peak by collimation does not produce a perfectly sharp edge as would be expected from two-body kinematics. This is because a collimator cuts on radius at some fixed position which translates into a cut on emission angle only in an approximate way, and is why the curves in figure 4.9 are labelled by their collimator size and distance individually rather than their ratio which is the approximate collimation angle. Multiple scattering by the electron in the radiator prior to emission and beam spot size and divergence are the major contributors to the error involved in interpreting a collimator as a cut in emission angle. All of these effects have been incorporated into the analytical calculation of the yields from a collimated coherent bremsstrahlung source that has been used in preparing this report. Crystal imperfections, which amount to an intrinsic spread in the direction of the incoming virtual photon, are also accounted for in the calculation.

Third, note that the relatively weak collimation at $5mm$ reduces the incoherent background without significantly affecting the coherent flux near the maximum, and thereby almost doubling the polarization of the beam at the peak relative to the uncollimated case. Further reducing the collimator diameter continues to narrow the peak and reduce the incoherent flux relative to the peak, albeit at some cost in peak intensity. In the case of the $2mm$ collimator, the peak polarization is essentially that of the coherent component alone. Although almost all of the photon beam energy is being absorbed at this point at the collimator, provided there is adequate shielding around the collimator the necessary flux in the collimated beam can be made up by increasing the electron beam current. The peak in figure 4.9 for a $2mm$ collimator contains 1M photons/s for an electron beam current of 100nA, which could be increased by a factor of up to 100 in the facility being planned for HALL D .

Fourth, note that the rate seen in the focal plane of the tagging spectrometer corresponds to the dotted curve in figure 4.9 , regardless of the collimation. This means that collimating the bremsstrahlung beam increases the rate in the tagger focal plane relative to what is seen at the detector. For example, running with the $2mm$ collimator and 10^7 photons/s in the main coherent peak implies according to figure 4.9 a rate of 250MHz per GeV in the focal plane. Under these conditions, only a small part of the focal plane is in coincidence

with the events of interest, which limits the rate of accidental tags to a reasonable level. For maximum flexibility, the full upper 25% of the tagging range must be designed to handle rates as high as this.

The net polarization of the beam under different collimation conditions is shown in figure 4.10. The dashed curves show how the maximum polarization in the peak varies as the peak energy is changed by rotating the crystal. The polarization in all cases is zero at the endpoint. Without collimation it rises as $(k-E)^2$, one power coming from the intensity of the coherent peak relative to the incoherent component going to zero linearly at the endpoint, and the other from the intrinsic polarization of the coherent photons also behaving like $(k-E)$ near the endpoint. Collimation allows one to essentially isolate the coherent component, so that the polarization available to the experiment rises from zero at the endpoint in a linear fashion. The dashed curves in figure 4.10 demonstrate this point.

4.6.2 Choice of radiator

The ideal radiator would be a layered structure with a strong transverse fields that alternate between layers spaced about $50nm$ apart, thus simulating the standing wave in a cavity driven by a 15eV laser. While it is possible to construct ordered materials with unit cells as large as this, the self-shielding of atoms means that beyond the atomic length scale the residual fields are comparatively weak. Hence heterogeneous structures are not viable for use as a coherent radiator. Since the strong fields inside a solid are revealed at the atomic scale, the first requirement for a good radiator is that the unit cell be compact and closely packed. The best radiators are those with the smallest unit cells because these provide the best match between the atomic and the crystal form factors. This match is best for the light elements, and essentially prohibits the effectiveness of any materials heavier than carbon. An extensive survey of possible radiator materials is presented in Ref. [9]. In table 4.1 is shown the figure of merit that those authors report for favored crystalline materials. The figure of merit is the product of the atomic times the crystal form factor evaluated at the leading peak, normalized to the value for diamond.

Table 1 shows that the list of viable materials for a crystal radiator is relatively short. Silicon would be an excellent choice from the point of view of price and fabrication, but unfortunately it is far inferior in terms of performance. Beryllium carbide is not a material that is familiar to the crystal growth industry, and nothing is known at present concerning its suitability for the growth of single crystals of large area. In general compound materials are

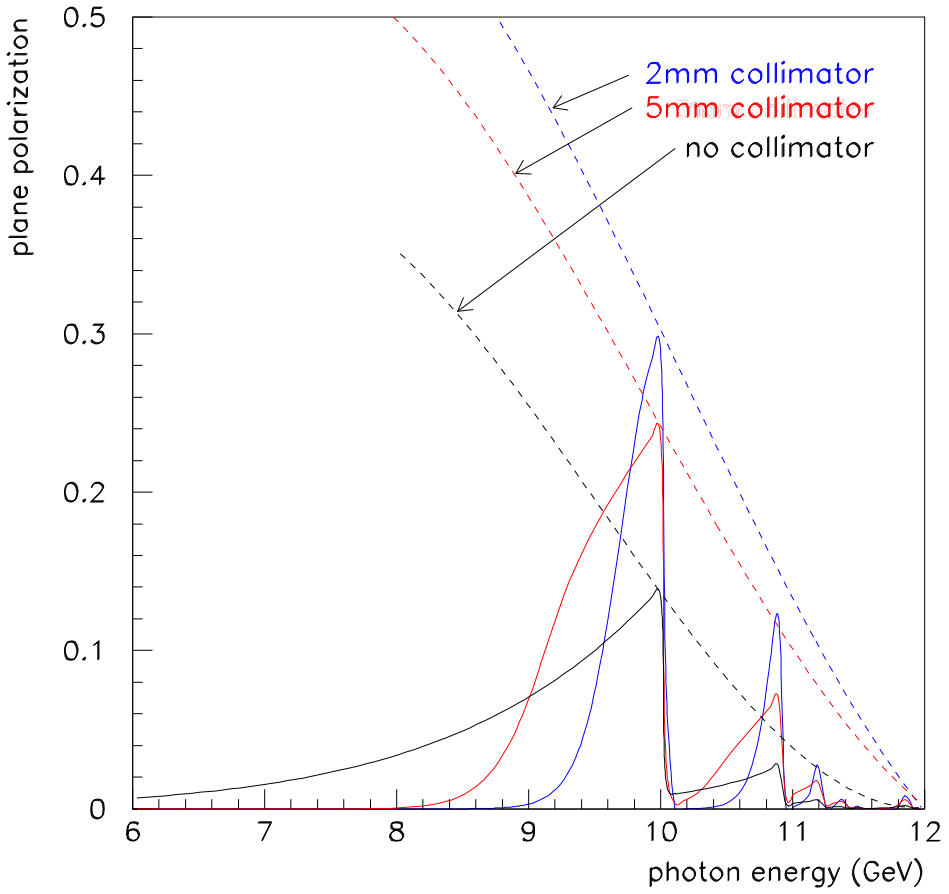

Figure 4.10: Plane polarization of the coherent bremsstrahlung beam, calculated under the same conditions as in figure 4.9. The dashed lines indicate the trajectory of the peak polarization as the peak energy is swept across the focal plane by rotating the crystal.

crystal	best reciprocal vector	$P/P_{diamond}$
diamond	2,-2,0	1.00
beryllium	0,0,2	0.86
boron	2,0,8	0.38
silicon	2,-2,0	0.19
Be_2C	2,2,0	1.10

Table 4.1: Figure of merit of various materials that might be used as a coherent bremsstrahlung radiator. This table is reproduced from Table 2 in H. Bilokon *et al.*

more susceptible to radiation damage than are pure elements, which would argue in favor of diamond and beryllium metal. These two materials are comparable in terms of their performance. Most of the experience to date with coherent bremsstrahlung has been with diamond radiators. Extensive expertise for handling large diamond crystals exists within the gem industry. High quality monocrystals of $6mm \times 6mm$ and as thin as $100\mu m$ were obtained at SLAC [8]by cleaving from a facet of a large gem. This was made possible by a contact that existed at the time with a friendly insider in the gem business. It is not clear at the present whether this success could be repeated in a cost effective way, and so it is important to consider beryllium as an alternative radiator material.

Beryllium metal is widely used in industry, being preferred for its high strength-to-weight ratio and robustness, in addition to its transparency to X-rays. Thin films of high-purity beryllium are routinely produced for vacuum window applications, which use some of the same vacuum deposition techniques that would be used for the growth of single crystals. As a radiator material, beryllium is distinguished as the metal with the highest Debye temperature, around 1400°K . The Debye temperature measures the temperature at which the thermal motion of the atoms in the lattice reaches the level of the zero-point motion due to their confinement in the lattice, as dictated by the uncertainty principle. A high Debye temperature indicates a stiff crystal lattice, in which the atoms have little liberty to move and so have large momentum fluctuations, as dictated by the uncertainty principle.

A high Debye temperature is important for a bremsstrahlung radiator material for three reasons. First, the cross section for coherent bremsstrahlung from a discrete crystal momentum vector $\vec{q}$ contains a factor $e^{-q^2/4M\theta_D}$ which

reflects the fact that position fluctuations of atoms in the lattice diminish the coherent effect. This factor is near unity for the low-order crystal momenta provided that θ is sufficiently large. Second, the Debye temperature is, roughly speaking, a measure of the stability of the crystal structure and hence its readiness to form as a single crystal and to survive significant doses of radiation. Third, the radiator material will inevitably be heated by the beam, and will normally operate in vacuum well above the ambient temperature. A high Debye temperature means that there is a large range of temperatures over which the material may operate without degraded performance as a crystal radiator. The Debye temperature of diamond is about 2200° K. Past experience has shown that diamond meets all of the requirements for a good crystal radiator. There is good reason to believe that beryllium would function almost as well at substantially less cost, but this remains to be proved.

4.6.3 Crystal thickness

The range of permissible thicknesses for a crystal radiator is bounded both from above and below. It is bounded from above by multiple scattering of the electron beam as it passes through the radiator, which causes the divergence of the incident beam to grow, thereby enlarging the photon beam spot on the collimator face and degrading the degree to which collimation discriminates against the incoherent component in favor of the coherent part. It is bounded from below by the fact that the crystal must be of some minimum thickness in order to achieve the full coherent gain. In the calculation of the coherent bremsstrahlung process one begins by assuming an infinite crystal, although practically it is presumed to mean only that the crystal is large compared to the some characteristic scale. It is important to identify what the characteristic scale is in this problem in order to know how thin one can make the crystal without hurting performance. In the analogous case of the Mosbauer effect, one can estimate the number of atoms participating in the collective absorption by looking at the emission time of the photon (lifetime of the radiating transition) and asking how many nuclei lie within the envelop of the photon wave packet. In the coherent bremsstrahlung process, the lifetime of the radiating system is given in the lab system by the uncertainty principle and by how far the electron energy deviates from its on-shell value between absorbing the virtual photon and emitting the real one. The latter quantity is almost exactly given by q_z , the virtual photon momentum component along the incident electron axis, which means that the electron travels a distance $\lambda = \hbar c/q_z$ during the interaction. For a given coherent peak at normalized energy x in the photon

spectrum, the coherence length is given by

$$\lambda = \frac{2e(1-x)}{xm^2} \tag{4.6}$$

in units of $\hbar c$. From this simple argument one sees that the coherent gain goes linearly to zero at the endpoint, a result that is borne out by the full QED calculation. One also sees that the lower limit on crystal thickness imposed by the coherence length depends upon both the electron beam energy and the photon energy. For a 12 GeV beam energy and a 6 GeV coherent photon the coherence length is $18nm$, or about 50 unit cells for diamond. This shows that the coherence length does not impose a practical limit on how thin the radiator should be.

The effects of multiple scattering are best presented by showing the calculated spectra for various radiator thicknesses. The diamond radiators used at SLAC were cleaved at approximately $100\mu m$ and then milled down to about $50\mu m$ using ion bombardment. In figure 4.11 is shown the photon spectrum for a $20\mu m$ and a $100\mu m$ radiator to demonstrate the effect. The $100\mu m$ spectrum is scaled down by a factor of 5 to facilitate the comparison. The calculation assumed a $2mm$ collimator located 80m downstream of the radiator. The loss in normalized intensity with the thicker radiator, as well as the broadening of the left edge of the peak, is due to the enlarging of the photon beam spot on the collimator face from multiple scattering of the electron beam in the crystal prior to radiation. A $100\mu m$ diamond crystal is roughly 10^{-3} radiation lengths thick. It is reasonable to run with as thick a radiator as is permitted by multiple scattering considerations, in order to keep the beam current to a minimum and prolong as much as possible the lifetime of the crystal.

4.6.4 Crystal mount

It has already been shown that in order to achieve appreciable coherent gain the crystal must be oriented so that the coherent peaks appear well below the end point. Eqn. 4.5 then implies that the orientation must be such that the crystal momentum dotted with the beam momentum be of order m^2 . Given a p of 12 GeV and q of 10KeV, this requires that the two vectors must be within $100\mu r$ of perpendicular to each other and that, within a range of angles of that order, the coherent peak sweeps out nearly the full range in x from 0 to 1. Hence both the incident beam angle and the angle of the crystal radiator must be stable at the level of a few μr in order to have a stable photon beam for running. At least one of the two must be adjustable in steps that are small compared to $100\mu m$ in order to have the ability to position the coherent peak

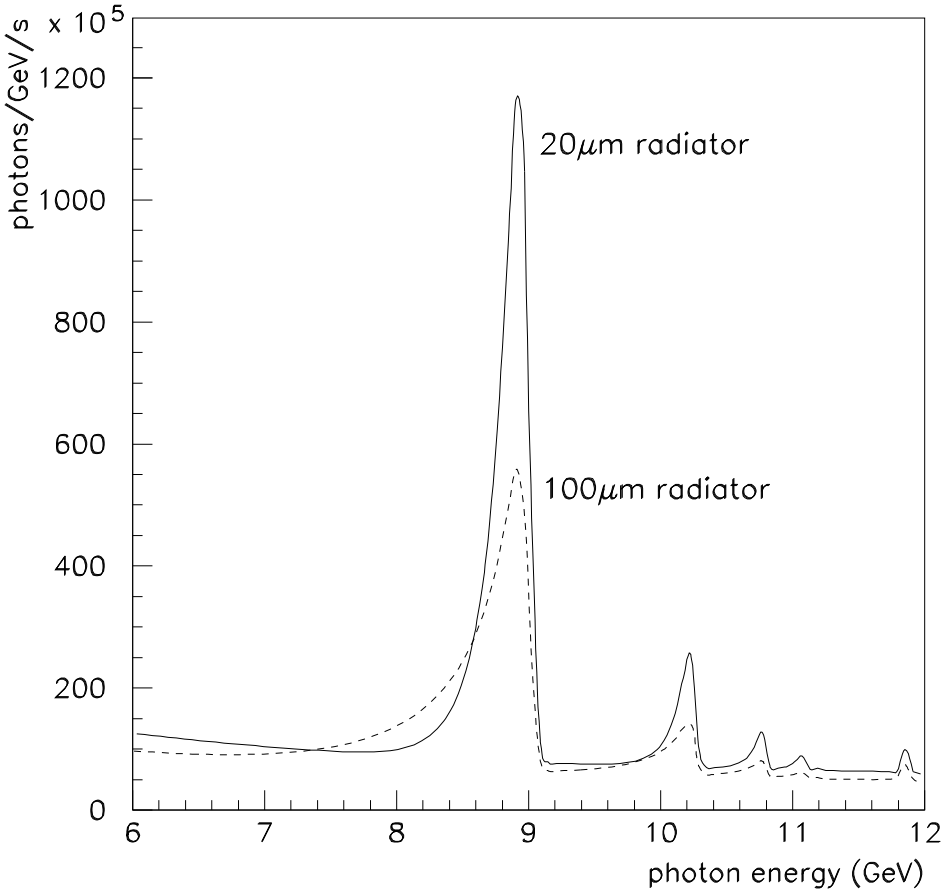

Figure 4.11: Collimated coherent bremsstrahlung spectrum from a 1A electron beam at 12 GeV using diamond radiators of two different thicknesses. The calculation assumes a $2mm$ collimator located 80m from the radiator, and typical values for beam emittance and crystal quality.

at the desired energy. These requirements are most simply achieved using a precision two-axis goniometer. Commercial devices of this type exist with step sizes as small as required for this application. With two-axis remote control the crystal can be reoriented in a matter of minutes to produce a coherent beam of any desired energy and in either vertical or horizontal plane polarization modes.

Thermal effects in the crystal mount and small variations in the beam tune from the accelerator make long term stability and reproducibility more difficult to achieve than adequate controls for the initial setup. For this reason it is important that there be sufficient diagnostics present to monitor the crystal orientation relative to the beam. This diagnostic is provided by the rates in the tagger focal plane counters. From figure 4.8 it is clear that the critical angle between the beam and the crystal, as well as the quality of the crystal, are accurately reflected in the position and sharpness of the coherent edge in the focal plane rate profile. Better than simply monitoring the critical angle, the tagger profile provides a direct look at the photon beam spectrum prior to collimation. This means that there is no need for an absolute alignment of the crystal and goniometer to this level of precision, because only relative accuracy is required. The second angle is non critical, typically of order a degree, and does not need to be monitored. If conditions require it, a feedback system could be put in place to correct for drifts seen in the tagger focal plane profile by periodically adjusting the goniometer setting within predefined limits. This would involve a slow control system, and does not need to be designed in advance.

4.6.5 Crystal quality and lifetime

There are two considerations that fall under the heading of crystal quality. The first respects the quality of the original crystal, and the second is with regard to degradation from radiation damage. In the calculation of the coherent bremsstrahlung spectrum a perfect single crystal was assumed, but even the very best crystals have some dislocations and other defects. Besides locally disrupting the regularity of the crystal, these defects impose stresses which produce small ripples in the crystal planes. If these ripples were amplified, the surface of a crystal would appear like a mosaic of planar regions with approximately parallel surfaces. The scale of deviations from planarity across the face of a single crystal is termed the *mosaic spread* of the crystal. The mosaic spread contributes in the same way as beam divergence to the smearing in the exact energy-angle relation for coherent photons. This quantity, which can be measured directly using specialized optical equipment, was poorly known by

the SLAC group for their diamonds, but they believed them to be better than $50\mu r$. This is the value that is used in the calculations for this report.

The SLAC group found that the performance of their diamonds had degraded considerably after a total charge of 3 Coulombs had been accumulated over a surface of $6mm \times 6mm$ in area. They were able to recover a better performance for the damaged crystals by putting them through an annealing process. This translates to five weeks of running, or about a two months of real time at $1\mu A$ of current, before the crystal would need to be removed for treatment. A small set of radiators of different thicknesses would accommodate a run plan that includes some running with maximum polarization, i.e. narrow collimation, a thin radiator and microamps of beam current, and running the rest of the time with a thicker radiator, less beam current and more modest collimation.

4.7 Electron Beam Line

The possibility of a collimated coherent bremsstrahlung photon source in HALL D depends in a critical way on having a low-emittance electron beam from CEBAF at 12 GeV. It is inevitable that, as the energy of the machine is increased, there will be some growth in the emittance from the steep rise in synchrotron radiation. However, the plans for the upgrade of the accelerator include measures that substantially control and offset these effects, albeit at substantial cost for some of them. Such investments require careful justification in terms of the physics research that they enable. The purpose of this section is to show the connection between the parameters of the beam at 12 GeV and the quality of the photon beam that can be produced from it for the HALL D . The connection between the photon source performance and the physics HALL D is planning to do is made elsewhere in this document. Any decision regarding the final configuration of the machine involves a cost/benefit analysis that goes beyond any one experimental hall. However, we see an important link between the HALL D project and the upgrade of CEBAF to 12 GeV beams. In the following sections the mutual implications of the two projects are explored in detail.

4.7.1 Beam emittance requirements

Widely different machine performance figures can be projected from the present performance to operation at 12 GeV, depending upon what other upgrades accompany the addition of high-gradient cavities to the linacs. Rather than

decide on some favorite configuration and base the HALL D design on that, we have decided to take the present parameters for operation at 6 GeV as a starting point, and examine how the photon beam is affected as the emittance gets worse. For this starting point, a value of $10mm \cdot \mu r$ is taken for the beam emittance at the entrance to the bremsstrahlung radiator. The definition of emittance used here is the area of the 2σ ellipse in the space of displacement from beam center *vs* divergence from the beam axis. Because synchrotron radiation occurs mainly in the horizontal plane inside the accelerator, the emittance values in x are generally larger than those for y. The calculations presented here assumed the same value for vertical and horizontal emittance, taking $10mm \cdot \mu r$ as an effective average between the two. The longitudinal emittance, displacement along the beam from bunch center *vs* deviation from nominal beam energy, is not a critical parameter for HALL D . Energy resolution of 25MeV f.w.h.m. for a 12 GeV beam or better is required in order to make full use of the resolution planned for the tagger.

The place where transverse emittance plays a critical role is at the photon collimator. For optimum effectiveness in collimation it is important that the electron beam spot at the collimator position be as small as possible. The electron beam does not actually reach the photon collimator, being bent into the dump shortly after the radiator by the tagger magnet. But considering the optics of the electron beam as if the tagger dipole were switched off, the electron beam at the radiator can be projected forward 80m to form a virtual image on the collimator entrance plane. The position and size of this spot gives the the definition of the 0° emission angle for the photons. If this spot is small compared to the collimator aperture and is centered then the collimator does its job of removing photons with emission angle beyond the collimator half-angle. However, if the virtual spot is larger than the aperture then the collimator serves only to reduce the intensity of the beam and does not discriminate between coherent and incoherent beam components.

Note that this analysis does not place any specific limits on the size of the beam at the radiator. The beam spot can and should be larger there to avoid burning a hole in the radiator. For the SLAC coherent bremsstrahlung source the beam at the radiator was $6mm$ in diameter and focused to image a $2mm$ spot at the collimator positioned 91m downstream of the radiator. The focus ensures that photons emitted near zero degrees, even those far from the beam axis at the radiator, will pass near to the axis at the collimator position and so be seen at the experimental target. The virtual electron beam spot is not the same as the actual photon beam spot on the collimator, which is concentric with the former but larger.

Figure 4.12 shows how the collimated photon spectrum depends upon the

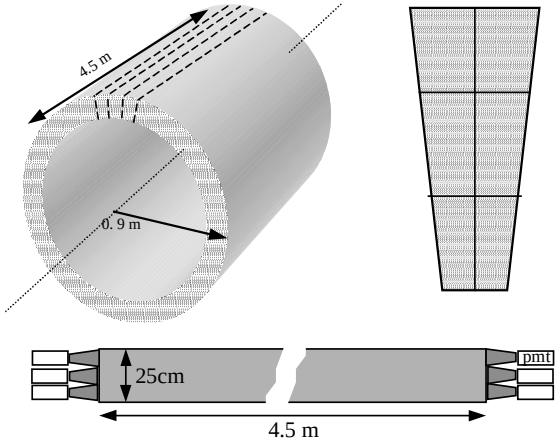

Figure 4.12: Coherent photon spectrum for three different values of the r.m.s. size of the virtual electron beam spot on the collimator. A $2mm$ diameter collimator 80m downstream of the radiator was used.

r.m.s. size of the virtual electron beam spot on the collimator. When the spot size becomes comparable with the collimator aperture then the collimation is rendered ineffective, and the photon spectrum and polarization revert to their uncollimated values. The connection between focal spot size and beam emittance can be seen by noting that an upper bound is placed on the angular divergence of the beam at the radiator in order to maintain the same incidence angle with respect to the planes of the crystal for all electrons in the beam. Practically, the divergence does not broaden the coherent peak provided that it is kept below the mosaic spread of the crystal. A conservative value for the allowable angular divergence δ in the electron beam at the radiator would then be $20\mu m$. Taken together with a $200\mu m$ r.m.s. spot size at the focus, this leads to an emittance of $50mm \cdot \mu r$ at 12 GeV. The $600\mu m$ spot size in figure 4.12 corresponds to an emittance of $150mm \cdot \mu r$ and the $2mm$ spot to $0.5mm \cdot mr$.

4.7.2 Electron beam line optics

Taking the electron beam out of the machine and focusing it onto a $200\mu m$ spot requires some optics in the beam line leading up to the radiator. Translating the beam emittance into a r.m.s. values for the beam radius and divergence requires the knowledge of the β parameter, defined as the ratio of the r.m.s. beam size at the focus to its angular divergence. The β varies along a beam line wherever there are focusing elements. When it comes out of the accelerator, β is large, of order 1km, corresponding very highly parallel beam. In order to focus a beam of emittance $50mm \cdot \mu r$ down to a r.m.s. size of $200\mu r$, the β must be reduced from 1km down to 10m by the use of focusing elements. The focusing must be done in both x and y axes separately to achieve the desired result, and must be accomplished by elements located along the transfer line from the accelerator vault to the surface. The strong focusing requirement significantly complicates the design of the transfer line, and will require careful study. It may be simpler to achieve a lower emittance beam and run with weaker focusing than to require a fine tuning in the transfer line in order to squeeze a larger emittance beam all the way down to its theoretically minimum focus.

Not only must the virtual electron spot be small enough to fit within the collimator aperture, but it must also be centered on the aperture and stable. In order to maintain a stable beam position on the collimator, the SLAC experiment [8] installed a segmented halo detector just upstream of the collimator and operated an active feedback loop to a vertical and horizontal pair of dipoles located just upstream of the radiator. From that distance a bend of

only $10\mu r$ results in a shift of $1mm$ at the collimator position. Hence the beam alignment feedback system is effectively decoupled from the crystal orientation controls. Small deflections that are necessary to keep the beam centered on the collimator do not produce appreciable walk in the beam-crystal angle, and by using a goniometer to control the latter, the former can be operated in a feedback circuit that operates independent of the photon source energy controls. The experimental program in parity violation at Jefferson Lab has already designed a position stabilization circuit that is able to keep the beam position steady to within $20\mu m$ over a 20m lever arm. A less sophisticated version of this circuit should be a part of the collimated photon source for HALL D .

4.7.3 Electron beam dump

The electron beam is dumped in the horizontal plane, as shown in figure 4.7. The horizontal bend offers several advantages over dumping the beam into the ground. The tagger magnet is easier to support if it sits in the horizontal position. It is also easier to mount and service the focal plane in this position. The dump itself is also more accessible in case it needs to be serviced. An above-ground dump also affords the possibility of running parasitic beam dump experiments that do not interfere with the operation of the experimental hall. It also allows for a possible future implementation of secondary meson beams in HALL D , which is the subject of the next section.

The primary design requirement for the electron beam dump is that it have a sufficiently high capacity to handle beams of the highest intensities foreseen for HALL D . A 250KW design would provide a a healthy margin for 12 GeV operation and sufficient capacity to handle as much as $10\mu A$ in the planned 24 GeV era. The present design calls for a 15° bend in the horizontal plane from the axis along which the electron beam enters the tagger building to the direction it exits into the beam dump. The total 15° bend is divided about equally between the tagger magnet and one or two dipoles. The dipoles were added as a cheaper alternative to enlarging the tagger magnet. It is considered that 15° provides sufficient space for shielding that the experimental hall can be effectively isolated from the dump.

4.7.4 Possibility of hadron beams

The physics program planned for HALL D centers around photoproduction as a source of both conventional and exotic mesons, and emphasizes the interest of these studies as follow-up to the experimental progress that has been

achieved over the last five years using pion and antiproton beams at hadron facilities. The possibility of using high energy electrons from CEBAF to generate secondary meson beams at some time in the future has arisen in HALL D discussions, however, mainly for two reasons. The first is that the detector that is being planned for HALL D is of a general-purpose design. At present very little is known concerning high energy meson photoproduction, aside from the fact that it is a prolific source of vector mesons and possibly of vector hybrids. The detector package described in this report is capable within the first two years of operation of collecting as much data on photoproduction as presently exists for any production mode, including pion production. Thus the possibility is very real that after a relatively short running period in HALL D , there might be reason to turn again to pion or kaon production methods to examine states that are suppressed or missing in photoproduction. The second reason is that one of the most successful programs ever carried out in meson spectroscopy was the LASS experiment, which used a secondary kaon beam generated using 20 GeV electrons from SLAC to study kaon production. The fact that the same detector could be used for both kinds of beams, and that some mention has already appeared of energies even higher than 12 GeV at Jefferson lab, warrants a brief summary of these discussions in this report.

The LASS experiment took 3-4 kaons per pulse and about 120 pulses per second during normal operation, for a total of 300-500 kaons/s. Averaged over the duty cycle of the accelerator, this beam rate was achieved with an average electron beam current of $7\mu A$. They used rf separation to obtain a nearly pure kaon beam, which required a beam line of 150m, rather long compared to the mean decay distance of about 40m for a 10 GeV K^- . A beam line of a similar design but without rf separation would fit into the HALL D design, with the production target just before the electron beam dump and the secondary beam being bent by a chicane onto the same axis as the photon beam. The 80m space between the tagger building and the experimental hall would allow room for one or more gas Cerenkov counters that could be used in the place of rf separation to tag the different species in the beam. Using the same apertures as were used for LASS would give in excess of 1000 kaons/s and about a factor of 60 more rate in pions for a $10\mu A$ electron beam. The secondary particles have a broad energy spectrum that peaks around half of the electron beam energy. While these rates are not high compared with what is available at a hadron machine, the availability of a high-quality detector designed for this kind of physics makes it worthwhile to carry out the design of the experiment and beam lines keeping this possibility in mind.

4.8 Tagging Spectrometer

4.8.1 Magnet

The tagging spectrometer being envisioned for HALL D is of a similar design to the one currently in use in Hall B. The radius of curvature has been adjusted to follow the path of the primary 12 GeV beam at a low field of only 1T. Operation at low field during the 12 GeV era allows the spectrometer to be used in the case of further energy upgrades, all the way up 24 GeV beam energy, simply by increasing the field in the dipole. Under this design the spectrometer is able to tag the top 50% of the photon spectrum (corresponds to the low momentum region in recoil electron momentum) independent of the energy of the primary beam. The choice to restrict the tagged region to 50% or more of the endpoint reflects the priority of the experimental program for running at the highest possible photon energies.

4.8.2 Focal-plane hodoscope

A plan view from above the tagger and focal plane is shown schematically in figure 4.13. The two primary requirements for the design of the focal plane hodoscope is that it have sufficient segmentation to provide the required photon energy resolution and that it be able to handle the high rates associated with coherent bremsstrahlung with collimation. Detector studies indicate that 0.1% r.m.s. photon energy resolution is required in the most demanding case, in order to make maximum use of the resolution of the detector to reconstruct incomplete events using the missing mass technique. Assuming that the energy of the incident electron beam is defined at the 0.1% level, a focal plane of non-overlapping counters each subtending a 25MeV bite of the total 6 GeV momentum tagged at 12 GeV electron beam energy provides the required tagged photon energy resolution. About 240 individual counters are required to completely instrument the tagger focal plane under these conditions. The detectors themselves can be little rectangular pieces of plastic scintillator no more than $2-3cm$ on a side and lined up with just enough overlap to prevent electrons from slipping between them without detection.

The counters subtending the upper 25% of the photon energy spectrum must be equipped with special bases and electronics to be capable of sustaining rates as high as 10MHz when running in collimated coherent mode. The part of the focal plane outside the coherent peak may as well be turned off for running in collimated mode because only the photons in the vicinity of the coherent peak are polarized. Given that one has a measurement of the energy

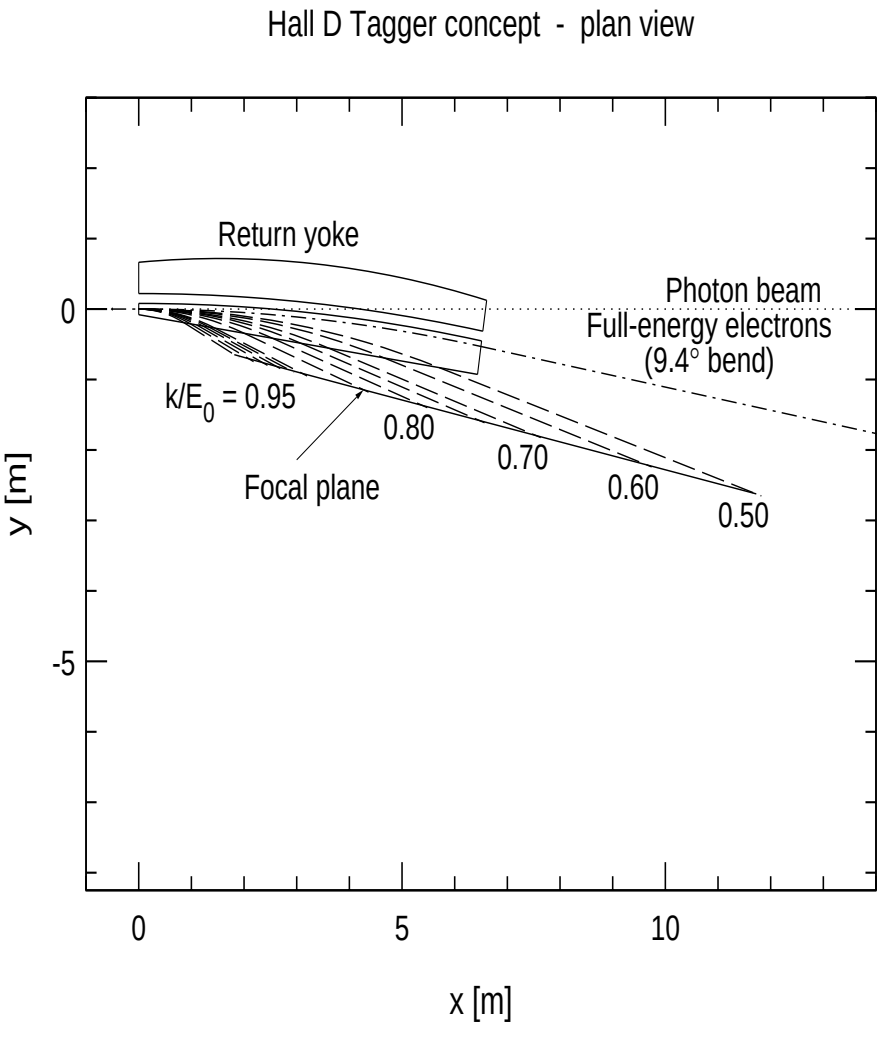

Figure 4.13: A plan view of the tagging spectrometer from above, showing the path of the primary beam and the trajectory of post-bremsstrahlung electrons of various recoil momenta.

of the photon from the tagger in any case, the primary reason for collimating the coherent beam is to enhance the polarization.

List of Figures

List of Tables

Bibliography

[1] N. Isgur and J. Paton. *Phys. Rev.*, D**31**:2910, 1985.

[2] T. Barnes. In *Physics with 8+ GeV Photons Workshop*. Workshop in Bloomington IN, July 14-16 1997, proceedings available from Jefferson lab.

[3] K. Schilling, P. Seyboth, and G. Wolf. On the analysis of vector meson production. *Nucl. Phys.*, **B15**:398, 1970.

[4] P. R. Page A. Afanasev. Photoproduction and electroproduction of $j^{PC} = 1^{-+}$ exotics. *Phys. Rev.*, D **57**:6771, 1998.

[5] A. Afanasev and A.P. Szczepaniak. in preparation.

[6] G.S. Adams *et al. Phys. Rev. Lett.*, **81**:5760, 1998.

[7] C. Keppel. Development of a Compton-backscattered photon source for Hall B at Jefferson Lab. In *Physics with 8+ GeV Photons Workshop*. Workshop in Bloomington IN, July 14-16 1997, proceedings available from Jefferson lab.

[8] W. Kaune, G. Miller, W. Oliver, R.W. Williams, and K.K. Young. Inclusive cross sections for pion and proton production by photons using collimated coherent bremsstrahlung. *Phys. Rev.*, D **11**(3):478–494.

[9] H. Bilokon, G. Bologna, F. Celani, B. D'Ettorre Piazzoli, R. Falcioni, G. Mannocchi, and P. Picchi. Coherent bremsstrahlung in crystals as a tool for producing high energy photon beams to be used in photoproduction experiments at CERN SPS. *Nuclear Inst. and Meth.*, **204**:299–310.